

Do radiative losses determine the characteristic emission of the blazar Mkn 421?

C. Baheeraj^{1*}, S. Sahayanathan^{2,3†}, Frank M. Rieger^{4,5}, Sitha K Jagan¹ and C. D. Ravikumar¹

¹ *Department of Physics, University of Calicut, Malappuram, Kerala, India*

² *Astrophysical Sciences Division, Bhabha Atomic Research Centre, Mumbai - 400085, India*

³ *Homi Bhabha National Institute, Mumbai 400094, India*

⁴ *Institut für Theoretische Physik (ITP), Universität Heidelberg, Philosophenweg 12, 69120 Heidelberg, Germany*

⁵ *Max-Planck-Institut für Kernphysik, P.O. Box 103980, 69029 Heidelberg, Germany*

Accepted XXX. Received YYY; in original form ZZZ

ABSTRACT

The radiative loss interpretation for the broken power-law spectra of blazars is often questioned since the difference between the indices does not support this inference. Using the blazar Mkn 421 as a case study, we performed a detailed analysis of its characteristic photon energy where the spectral index changes significantly. We used the observations of the source by *Swift*-XRT from 2008 to 2019 to identify the characteristic photon energy and the corresponding spectral indices. The spectra in the energy range 0.3–10.0 keV can be well fitted by a log parabola as well as a smooth broken power-law. From the smooth broken power-law spectral fit we show that the spectral indices before and after the characteristic photon energy are strongly anti-correlated. Further, the spectral curvature measured at the characteristic photon energy indicates an anti-correlation with the low energy spectral index while the high energy spectral index shows a positive correlation. These findings are at variance with a simple radiative loss interpretation for the characteristic photon energy, and alternative scenarios are thus discussed. Though these scenarios are in principle capable of reproducing the correlation results, they deviate significantly from the observed properties.

Key words: galaxies: active – BL Lacertae objects: individual: Mkn 421 – X-rays: galaxies – galaxies: jets – radiation mechanisms: non-thermal

1 INTRODUCTION

The BL Lac object Mkn 421 is one of the nearest ($z = 0.031$) and extensively studied blazars with a non-thermal spectrum extending from radio to very high energy gamma rays (Acciari et al. 2009; Abdo et al. 2011; Aleksić et al. 2012; Baloković et al. 2016; Bartoli et al. 2016). The source exhibits rapid flux and spectral variability, suggesting the emission to originate from a relativistic moving jet aligned close to the line of sight (Dondi & Ghisellini 1995). Its broadband spectral energy distribution (SED) is characterized by two broad peaks, where the low-energy component is interpreted as synchrotron emission from a relativistic electron population (Celotti & Ghisellini 2008) while the high-energy component is usually attributed to inverse Compton scattering of the synchrotron photons by the same electron population (e.g., Aleksić et al. 2012; Abdo et al. 2011; Acciari et al. 2011). This synchrotron self Compton (SSC) interpretation of the high energy emission is further strengthened by the correlated X-ray – TeV flux variability with quadratic dependence (e.g., Mastichiadis & Kirk 1997; Błażejowski et al.

2005; Giebels et al. 2007; Fossati et al. 2008; Katarzyński & Walczewska 2010; Bartoli et al. 2011; Kapanadze et al. 2018a,b).

In general, different types of non-thermal electron distributions, mostly involving a power-law regime (e.g., broken power-law, power-law with exponential cut-off etc.), have been used to account for the broadband SED of blazars (e.g., Sinha et al. 2017; Kataoka & Stawarz 2016; Yan et al. 2013; Tramacere et al. 2007b; Krawczynski et al. 2004).

On the other hand, since the narrow band X-ray spectrum can deviate significantly from a simple power-law, the photon number distribution is often represented by a log-parabolic function

$$N(\epsilon) \propto \left(\frac{\epsilon}{\epsilon_0} \right)^{-\alpha - \beta \log(\epsilon/\epsilon_0)} \quad (1)$$

Here, ϵ is the photon energy, α is the spectral slope at energy ϵ_0 and β is the spectral curvature defined at the peak energy ϵ_p of the SED (Massaro et al. 2004; Tramacere et al. 2007b). In case of Mkn 421, ϵ_p falls into the soft X-ray regime and the hard X-ray energy band probes the decline of the synchrotron spectral component. The spectrum at these energy regimes individually can be reproduced by a log-parabolic function, though this approach is not very successful in explaining the

* E-mail: baheeraj314@gmail.com

† E-mail: sunder@barc.gov.in

combined optical/UV and X-ray spectra (Massaro et al. 2004; Tramacere et al. 2009; Sinha et al. 2015a)

The characteristic peak photon energy (ϵ_p) of Mkn 421, at which the synchrotron spectral component carries maximum power, can vary significantly depending on the source state. For instance, Kapanadze et al. (2020) showed that ϵ_p varies from < 0.1 to > 15 keV during different flux states using Swift-XRT observations. Such large variation in ϵ_p is also reported by various authors using *RXTE*, *BeppoSAX*, *XMM-Newton* observations (e.g., Massaro et al. 2004; Tramacere et al. 2007a). The spectral shape around ϵ_p is usually well represented by a log-parabola function. Correlation studies between the fit parameters on the other hand, are often contradictory or inconclusive. For example, ϵ_p and β obtained through the log-parabolic spectral fit of *BeppoSAX*, *RXTE*, *XMM-Newton* and *Swift*-XRT observations of Mkn 421 during 1997–2006 were found to be anti-correlated (Tramacere et al. 2007a; Massaro et al. 2008; Tramacere et al. 2009, 2011). However, no significant correlation between these quantities was witnessed in case of *Swift*-XRT observation during 2005–2008 (Kapanadze et al. 2018a), 2009–2012 (Kapanadze et al. 2018b), 2015–2018 (Kapanadze et al. 2020), and also in combination with *NuSTAR* observations during April 2013 (Sinha et al. 2015b). Similarly, Massaro et al. (2004) have reported a strong positive correlation between the spectral index at 1 keV and the curvature parameter using *BeppoSAX* observations (0.1–100 keV) of Mkn 421 during May 1999 and April–May 2000; however, *Swift*-XRT observations and combined *Swift*-XRT/*NuSTAR* spectra did not show an appreciable correlation (Sinha et al. 2015b; Kapanadze et al. 2017; Kapanadze et al. 2018a). In spite of this seemingly contradictory results, in many observations the enhancement in flux is associated with a spectral hardening commonly referred to as “harder when brighter” trend (Kapanadze et al. 2016; Kapanadze et al. 2017; Kapanadze et al. 2018a,b; Kapanadze et al. 2020).

The power-law/log-parabolic photon spectra demand the emitting electron distribution to be also power-law/log-parabola type (Kardashev 1962; Massaro et al. 2004; Tramacere et al. 2009). A power-law electron distribution can be readily achieved under Fermi acceleration (e.g., Rieger et al. 2007), while a log-parabolic electron distribution may indicate an energy-dependence in the particle acceleration and/or diffusion process (Massaro et al. 2004; Jagan et al. 2018; Goswami et al. 2018; Goswami et al. 2020). In particular, when the electron escape time-scale from the main particle acceleration site becomes mildly energy-dependent (referred to as ‘energy dependent diffusion model’, hereafter EDD), the resultant electron distribution has been shown to follow a log-parabola function (Jagan et al. 2018). On the other hand, when the energy-dependence is strong, the shape deviates from a log-parabola. The latter case is witnessed in the hard X-ray spectra of Mkn 421 (Goswami et al. 2018; Goswami et al. 2020) observed by *NuSTAR*. The spectra corresponding to different flux states can be well fitted by synchrotron emission originating from an electron distribution obtained in an EDD model with a strong energy-dependent escape time scale. Incidentally, the hard X-ray spectra can also be explained by a log-parabolic electron distribution and hence, single model fits of the source spectra does not allow one to differentiate between these two models. However, the fit parameters of the EDD model corresponding to the differ-

ent flux states indicate a strong correlation, while this is not the case with a log-parabolic electron distribution.

The peak spectral energy ϵ_p can be translated to a break or peak energy, $E_b = \gamma_b m_e c^2$, in the emitting electron energy distribution¹ under synchrotron theory. The system deposits most of its power to the electrons at this energy, and hence identifying the process that determines γ_b (or ϵ_p) is important to understand the dynamics of the source. Radiative cooling (synchrotron and/or inverse Compton) of a power-law electron distribution can give rise to a broken power law electron distribution with power-law indices differing by unity (Kardashev 1962). Correspondingly, the photon spectrum will also be a broken power-law with a difference of 0.5 between high and low energy spectral indices (Rybicki & Lightman 1986). However, SED modelling of blazars often does not support this inference and the index difference is frequently found to be significantly larger than 0.5 (e.g., Mankuzhiyil et al. 2012). On the other hand, radiative cooling of a log-parabolic electron distribution can transform the distribution into a broken log-parabolic form. This could probably explain the large differences between spectral indices (Jagan et al. 2018). Under this interpretation, the increase or decrease in the spectral slope at low energies ($< \epsilon_p$) will be associated with a similar spectral slope change at high energies ($> \epsilon_p$). In principle, the assumption of multiple acceleration processes is also capable of producing broken power-law electron distributions (e.g., Sahayanathan 2008). The low and high energy indices would then be governed by the associated acceleration rates.

In the present work, we examine the radiative loss origin of ϵ_p in the high energy peaked blazar Mkn 421. For this, we use long term observations of the source by *Swift*-XRT spanning from January 2008 to December 2019. The spectral resolution of *Swift*-XRT is appreciable within the energy range 0.3 to 10.0 keV, encompassing a broad range of ϵ_p , and hence, represents a suitable experiment to perform this study. The X-ray spectrum is well represented by a log-parabola function which allows one to constrain ϵ_p . The spectral indices before and after ϵ_p are obtained by refitting the spectrum with a smooth broken power-law. We then study the correlation between these quantities to explore the possible origin of ϵ_p .

The paper is organised as follows: In Section 2, we discuss the observation and data reduction procedure, while the X-ray spectral study and correlations between fitting parameters are described in Section 3. Discussion and summary of the work are presented in Section 4.

2 OBSERVATION AND DATA ANALYSIS

We analysed the *Swift*-XRT (Burrows et al. 2005) observations of Mkn 421 during 2008–2019. The data were retrieved from NASA’s HEASARC interface and processed using XRT-DAS software package (Version 3.0.0) included within HEASOFT package (Version 6.22.1). We used only those observations which were performed in Windowed Timing (WT)

¹ The electron energy distribution is represented by $E^2 N(E)$, where $N(E)$ is the specific electron number density. Most of the electron energy resides at E_b when the broken power law indices are > -2 and < -2 , respectively.

mode and selected events with 0–2 grades. Standard procedures employing *xrtpipeline* (Version v0.13.4) were used for calibration and data cleaning.

A circular region of about 20–30 pixel radius centred at the source was used to extract the source spectrum, while about 30–40 pixel radius circular region which is free from the source contamination was used to extract the background spectrum. For observations with pileup, the source spectra were extracted by excluding the central circular aperture of 2–3 pixel radius. The final spectrum was produced using *xrtproducts* (Version v0.4.2). The ancillary response files (ARFs) were generated using the XRTMKARF task and the latest response matrices files (RMF) were used from the *Swift* CALDB. To ensure better χ^2 statistics, the spectra were grouped to 20 photons per bin using the tool GRPPHA v.3.0.1. We rejected some observations that were strongly biased due to the dead columns on the CCD.

3 X-RAY SPECTRAL FIT

The X-ray spectra in the 0.3 – 10.0 keV energy band encompass or are close to ϵ_p , and hence are significantly curved. The reduced data is analysed with the XSPEC package (Arnaud 1996) using a log-parabolic function while fixing the hydrogen column density to the Galactic value $N_H = 1.92 \times 10^{20} \text{cm}^{-2}$ (Kalberla et al. 2005) for all the observations. Since our aim is to understand the origin of ϵ_p , we used the *eplogpar* model (Tramacere et al. 2009) to perform the spectral fit. The log-parabolic function under this model is expressed in terms of ϵ_p as

$$N(\epsilon) \propto 10^{-\beta (\log(\epsilon/\epsilon_p))^2} / \epsilon^2. \quad (2)$$

We excluded observations having large reduced chi-squared ($\chi_{\text{red}} > 1.2$); however, for some observations we have extracted spectra from individual orbits to obtain a better fit. Certain observations corresponding to a single orbit were also divided segment-wise to improve the spectral fit. The details of the observation are shown in Table 1. For many observations, the obtained ϵ_p lies outside the 0.3 – 10.0 keV range. These estimates are not reliable, since they fall outside the spectral energy range of *Swift*-XRT and are thus excluded. This leaves 258 spectra with ϵ_p between 0.4 to 7.0 keV for the present study. Consistent with the literature (Massaro et al. 2004; Tramacere et al. 2007a; Kapanadze et al. 2016; Kapanadze et al. 2017), the spectra in this energy regime can be well fitted by a log-parabola. In Table 1 (column 4–5), we provide the fit results and in Figure 1 (upper panel) we show the scatter plot between ϵ_p and β . The Spearman rank correlation study between ϵ_p and β yields $r = -0.28$ with a null hypothesis probability of 1.35×10^{-05} . This result is consistent with earlier studies where a weak or no correlation was observed (Kapanadze et al. 2018a,b; Sinha et al. 2015b).

The radiative loss interpretation of ϵ_p predicts the spectral slopes at energies $\epsilon \ll \epsilon_p$ and $\epsilon \gg \epsilon_p$ to be positively correlated. To examine this, we fitted the spectra with a smooth broken power-law function defined by

$$N(\epsilon) \propto \left[\left(\frac{\epsilon}{\epsilon_b} \right)^{\Gamma_{\text{low}}} + \left(\frac{\epsilon}{\epsilon_b} \right)^{\Gamma_{\text{high}}} \right]^{-1} \quad (3)$$

where Γ_{low} and Γ_{high} are the indices before and after the break energy ϵ_b . The peak of the smooth broken power-law function in $\epsilon^2 N(\epsilon)$ representation is

$$\epsilon_{p,\text{sbpl}} = \epsilon_b \left(\frac{\Gamma_{\text{high}} - 2}{2 - \Gamma_{\text{low}}} \right)^{\frac{1}{\Gamma_{\text{low}} - \Gamma_{\text{high}}}}. \quad (4)$$

For typical values of Γ_{high} (~ 2.5) and Γ_{low} (~ 1.5), $\epsilon_b \approx \epsilon_{p,\text{sbpl}}$. The function (3) was added as a local model (*sbpl*) in XSPEC and the 0.3 – 10.0 keV *Swift*-XRT observations of Mkn 421 were refitted. However, the narrow-band X-ray spectra do not allow us to sufficiently constrain all parameters of the model. Hence, we performed a fitting with ϵ_b fixed to the value ϵ_p obtained from the *eplogpar* spectral fit. A subsequent inspection shows that $\epsilon_{p,\text{sbpl}}$ estimated from equation (4) using the so obtained best fit Γ_{low} and Γ_{high} does not differ much from ϵ_p (Figure 2), suggesting that our choice of ϵ_b does not strongly affect the outcome. We consider only those *Swift*-XRT observations with $0.4 \text{ keV} < \epsilon_p < 7.0 \text{ keV}$ since estimation of Γ_{low} and Γ_{high} demands ϵ_p to be within the spectral energy range of *Swift*-XRT. The resultant best fit values for Γ_{low} and Γ_{high} are given in Table 1 (column 7–8), while the scatter plot between these quantities is shown in Figure 3. The correlation study between these quantities yields a linear correlation coefficient $r = -0.95$ with significance, $p > 99.99$ per cent (Press et al. 1992). This strong anti-correlation between Γ_{low} and Γ_{high} poses a serious challenge to a simple radiative cooling interpretation of ϵ_p . A linear fit to Γ_{low} and Γ_{high} results in

$$\Gamma_{\text{high}} = (-0.89 \pm 0.05)\Gamma_{\text{low}} + (3.83 \pm 0.08) \quad (5)$$

with a goodness of fit (q-value) of 0.99. The inability of the simple radiative loss interpretation to successfully account for the origin of ϵ_p can be further visualized by studying the correlation between Γ_{low} or Γ_{high} with the curvature parameter β obtained from *eplogpar* model. In Figure 4 (bottom panel), we show the scatter plot between these quantities. The strong linear correlation of Γ_{high} with β ($r = 0.96$, $p > 99$ per cent) and anti-correlation of Γ_{low} with β ($r = -0.92$, $p > 99$ per cent) are consistent with the anti-correlation observed between Γ_{low} and Γ_{high} . A softening of the high energy index is associated with a hardening of the low energy index (broadening of the synchrotron spectral component). Correspondingly, high curvature β will be associated with hard Γ_{low} and steep Γ_{high} (narrowing of the synchrotron spectral component).

We did not find any appreciable correlation between Γ_{low} or Γ_{high} with the 0.3 – 10.0 keV integrated flux ($F_{0.3-10.0\text{keV}}$, middle panel of Figure 4). This indicates that the narrowing of the synchrotron component of the SED of Mkn 421 is not associated with flux state. This is also consistent with the weak correlation observed between β and $F_{0.3-10.0\text{keV}}$ (lower panel of Figure 1). Similarly, no significant correlation is witnessed between ϵ_p and Γ_{low} or Γ_{high} (top panel of Figure 4). Hence, the narrowing of the SED cannot be attributed to “bluer when brighter” trend of Mkn 421.

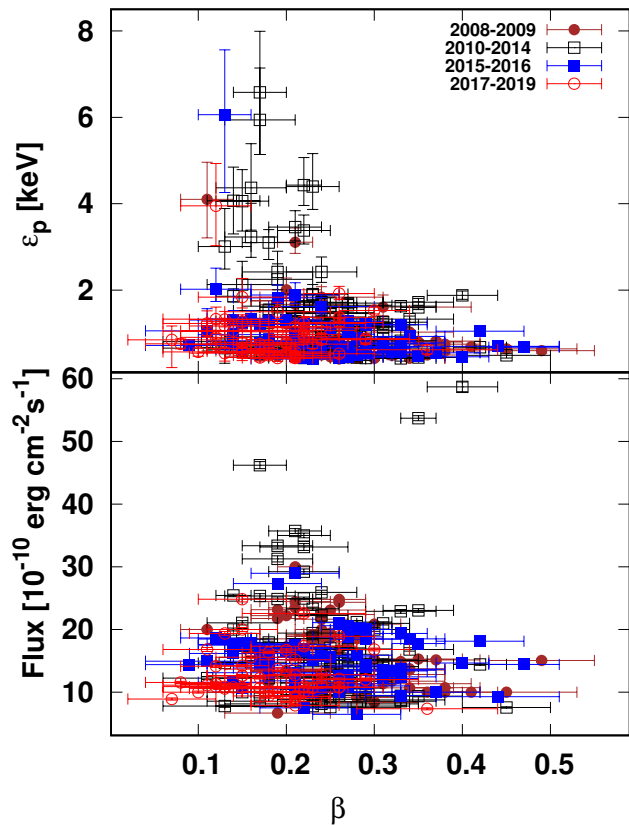
4 DISCUSSION AND SUMMARY

The observed anti-correlation between Γ_{low} and Γ_{high} is inconsistent with a simple radiative loss interpretation of ϵ_p . To examine alternate explanations, we consider the case where

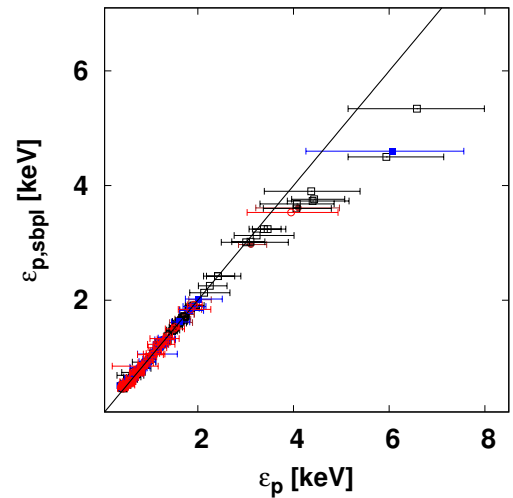
Table 1. Best fit parameters of spectral fitting using *eplogpar* model and *sbpl* model

ObsID (1)	Date of Obs. (2)	Exposure (sec) (3)	<i>eplogpar</i>			<i>sbpl</i>			Flux _{0.3–10.0 keV} (10^{-10} erg cm $^{-2}$ s $^{-1}$) (10)
			ϵ_p (keV) (4)	β (5)	χ^2_{red} (dof) (6)	Γ_{low} (7)	Γ_{high} (8)	χ^2_{red} (dof) (9)	
30352053-Orb2	2008-01-16	575.1	$0.42^{+0.07}_{-0.08}$	0.28 ± 0.05	1.04 (305)	1.36 ± 0.12	2.54 ± 0.02	1.06 (305)	20 ± 0.28
30352054	2008-01-16	1134.085	$0.42^{+0.04}_{-0.05}$	0.3 ± 0.03	1.08 (394)	1.33 ± 0.1	2.57 ± 0.01	1.12 (394)	15.26 ± 0.15
30352056	2008-01-17	944.126	$0.43^{+0.05}_{-0.07}$	0.34 ± 0.04	0.95 (322)	1.29 ± 0.12	2.61 ± 0.02	1.0 (322)	13.54 ± 0.17
30352055-Orb1	2008-01-17	394.9	$0.64^{+0.07}_{-0.08}$	0.45 ± 0.08	1.11 (227)	1.29 ± 0.12	2.69 ± 0.04	1.12 (227)	10 ± 0.21
30352055-Orb2	2008-01-17	362.6	$0.60^{+0.05}_{-0.04}$	0.49 ± 0.06	1.09 (260)	1.22 ± 0.1	2.73 ± 0.03	1.12 (260)	15.04 ± 0.26
30352058	2008-01-18	889.108	$0.57^{+0.04}_{-0.04}$	0.33 ± 0.04	1.07 (378)	1.38 ± 0.07	2.59 ± 0.02	1.1 (378)	14.88 ± 0.16
30352059	2008-01-19	919.112	$0.43^{+0.04}_{-0.04}$	0.34 ± 0.04	1.04 (359)	1.22 ± 0.12	2.62 ± 0.01	1.06 (359)	13.73 ± 0.15
30352060	2008-02-06	753.06	$0.60^{+0.05}_{-0.06}$	0.26 ± 0.03	1.13 (429)	1.48 ± 0.06	2.51 ± 0.02	1.15 (429)	24.33 ± 0.24
30352066	2008-02-10	1174.1	$0.74^{+0.03}_{-0.03}$	0.3 ± 0.03	1.17 (467)	1.46 ± 0.04	2.55 ± 0.02	1.18 (467)	20.85 ± 0.18
30352068	2008-02-11	1868.208	$0.46^{+0.03}_{-0.05}$	0.25 ± 0.02	1.1 (495)	1.44 ± 0.06	2.52 ± 0.01	1.14 (495)	18.61 ± 0.14

(Table is available in its entirety in the online version.)

**Figure 1.** The scatter plot between β and ϵ_p obtained from *eplogpar* (top panel) and between β and the integrated 0.3–10.0 keV flux (lower panel) for different epochs.

the synchrotron spectral component is governed by a power-law with an exponential cut-off. Such spectral shape could be possible when the underlying particle distribution has a sharp cut-off at the maximum achievable electron energy. The high-energy end of the synchrotron spectrum will then be governed by the exponential decay of the synchrotron single particle

**Figure 2.** The scatter plot between ϵ_p and $\epsilon_{p, sbpl}$ along with the identity line (see text). The symbols are as shown in Figure 1.

emissivity function. To mimic this, we assume a synchrotron spectral shape as

$$N(\epsilon) \propto \epsilon^{-\psi} \exp\left(-\frac{\epsilon}{\epsilon_c}\right). \quad (6)$$

The SED peak in $\epsilon^2 N(\epsilon)$ representation will be

$$\epsilon_{p, \text{exp}} = (2 - \psi)\epsilon_c, \quad (7)$$

so that the spectral slope of the photon distribution around $\epsilon_{p, \text{exp}}$ can be expressed as

$$\Gamma_{\text{exp}}(\epsilon) = \psi + \frac{\epsilon}{\epsilon_{p, \text{exp}}}(2 - \psi). \quad (8)$$

In this case, the spectral slopes at energies $\epsilon < \epsilon_{p, \text{exp}}$ and $\epsilon > \epsilon_{p, \text{exp}}$ will be anti-correlated. If we set $\epsilon_{p, \text{exp}} = 1.14$ keV corresponding to the average value of ϵ_p estimated from all the observations, the dependence of $\Gamma_{\text{exp}}(0.3 \text{ keV}) = \Gamma_{\text{low}}$ and $\Gamma_{\text{exp}}(10.0 \text{ keV}) = \Gamma_{\text{high}}$ can be studied for different values of ψ ($1.75 < \psi < 2.0$). In Figure 3, we show this dependence

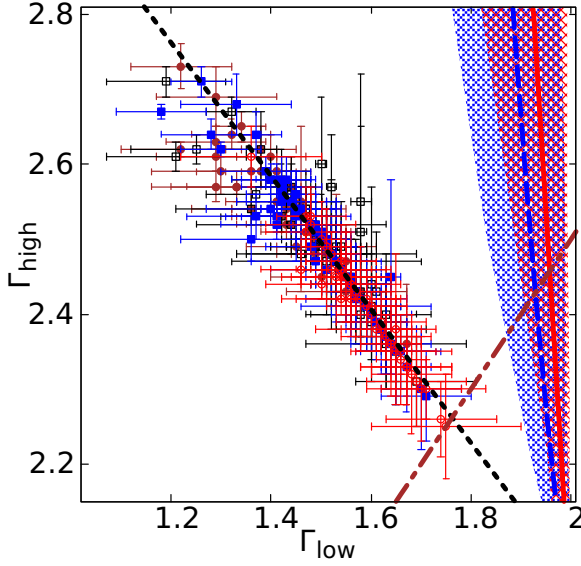


Figure 3. Scatter plot between Γ_{low} and Γ_{high} : black dotted line represents the best fit line of the observational Γ_{low} and Γ_{high} . The red solid line correspond to the synchrotron spectrum of an electron distribution of power-law with an exponential cut-off for $1.75 < \psi < 2.0$, and the red shaded region represents its $1\text{-}\sigma$ deviation. The blue dashed line correspond to the synchrotron spectrum of a electron distribution with a gradual decline at the maximum electron energy by varying ϕ between 1.3 and 2.0, and the blue shaded region represents its $1\text{-}\sigma$ deviation. The brown dotted dash line represents the cooling break. The symbols are as shown in Figure 1.

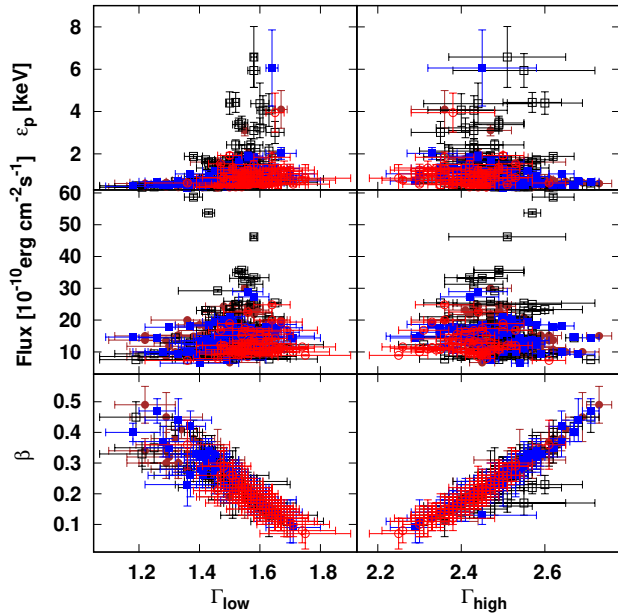


Figure 4. Left panel: scatter plot between Γ_{low} and curvature parameter β , 0.3–10.0 keV flux and ϵ_p ; Right panel: scatter plot between Γ_{high} and curvature parameter β , 0.3–10.0 keV flux and ϵ_p . The symbols are as shown in Figure 1.

as red solid line and the red shaded region represents its $1\text{-}\sigma$ deviation. Though this interpretation supports the anti-correlation between the indices, it deviates largely from the best fit line obtained from the observed Γ_{low} and Γ_{high} (using *sbpl*). *NuSTAR* observations of the source also do not support such an interpretation (Baloković et al. 2016).

Another possible explanation for ϵ_p could be, when the underlying particle distribution exhibits a gradual decline at the maximum electron energy rather than a sharp cut-off, that dominates the spectral shape around ϵ_p . To examine this possibility, we use the electron distribution accelerated at a shock front with constant acceleration and escape time scales (Kirk et al. 1998)

$$N(\gamma) \propto \gamma^{-(1+\phi)} \left(1 - \frac{\gamma}{\gamma_{\text{max}}}\right)^{\phi-1}. \quad (9)$$

Here, γ is the Lorentz factor of the electron, γ_{max} is the Lorentz factor corresponding to the maximum electron energy, and ϕ is the ratio of the acceleration and escape time scales. The observed synchrotron spectrum will then be (Rybicki & Lightman 1986)

$$N(\epsilon) \propto \frac{1}{4\pi} \int_{\gamma_{\text{min}}}^{\gamma_{\text{max}}} P_{\text{syn}}(\gamma, \epsilon^*) N(\gamma) d\gamma \quad (10)$$

where P_{syn} is the synchrotron single particle emissivity and ϵ^* is the photon energy in the comoving frame of the emitting region carried by the blazar jet (e.g., Begelman et al. 1984). The integration in equation (10) is performed numerically using quadrature, and we study the spectral shape around the peak. Again setting ϵ_p at 1.14 keV, the spectral index at 0.3 keV and 10 keV can be studied for different values of ϕ ($1.3 < \phi < 2.0$). In Figure 3, we show the plot between these indices as blue solid line and the blue shaded region represents the $1\text{-}\sigma$ deviation of the line. This interpretation for ϵ_p also supports an anti-correlation between Γ_{low} and Γ_{high} ; however, it still deviates significantly from the best fit line.

An alternative scenario which could be capable of reproducing the best fit straight line besides explaining the observed anti-correlation between Γ_{low} and Γ_{high} is when the synchrotron spectral component is a superposition of multiple broken power-law components. This would implicitly assume that the emission region is not reducible to a single homogeneous zone. The dominant broken power-law component then determines ϵ_p and with proper choice of break energy and/or the normalisation one could possibly reproduce the observed best fit straight line. However, unless some fine tuning occurs, one would also expect ϵ_p or the flux to be correlated or anti-correlated with Γ_{low} or Γ_{high} . The apparent absence of such correlations (top and middle panels of Figure 4) would again seem to disfavour simple variants of such a scenario.

As shown above, the curvature in the electron distribution introduced by the simplistic assumptions of constant acceleration and escape time-scales is unable to account for the observed properties. Probably, relaxing these assumptions, by including more complex energy-dependent acceleration and escape time-scales, could modify the correlation and reduce the deviation.

Multiple particle acceleration scenarios are also capable, in principle, of producing electron distributions that could imitate a broken power-law (e.g., Sahayanathan 2008). In this case, the indices are governed by the ratio of the accelera-

tion and escape timescales of the associated acceleration processes. The dominant acceleration processes in the blazar jet are assumed to be shock- and stochastic-type. Since the rate of acceleration by both these processes depends on the nature of particle diffusion into the jet medium, the corresponding particle power-law indices may be correlated. However, the exact nature of this correlation and comparison with observations would demand a detailed study/simulation of AGN jets considering these acceleration processes.

An important uncertainty in the present work is related to the choice of ϵ_b used in spectral fitting with the *sbpl* model. Since this parameter value has been frozen to ϵ_p obtained from the log parabola (symmetric function) spectral fit, this could introduce an additional bias which may be reflected in the parameters Γ_{high} and Γ_{low} . In order to explore this, we performed a combined spectral fit using simultaneous/near-simultaneous *NuSTAR* observations of the source. The *NuSTAR* data were downloaded from the online data archive² and standard data reducing techniques were employed using the latest software provided³. The spectral fit is then performed using *sbpl* model on simultaneous/near-simultaneous *Swift*-XRT (0.3–10.0 keV) and *NuSTAR* (3.0 to 30.0 keV) X-ray spectra with all parameters set free. It may be noted that, only four *NuSTAR* observations were simultaneous with *Swift*-XRT; dividing the later orbit-wise we obtain six spectra. The best spectral fit parameters are given in Table 2. We find that the $\epsilon_{p,\text{sbpl}}$ obtained through the combined spectral fit matches reasonably well with ϵ_p got from the log parabolic fit of *Swift*-XRT observations. The scatter plot between these quantities along with the identity line is shown in Figure 5. Though this result can be viewed as supporting our choice of ϵ_b , it is based on only a small number of data points. To improve on this and to be able to draw a more firm conclusion on the nature of ϵ_p , further simultaneous broad band X-ray observations of the source are clearly desirable. Nevertheless, the fact that all data points in Figure 3 lie above the cooling break line (brown dotted dash line) clearly disfavours a radiative loss interpretation of the considered, characteristic photon energy in Mkn 421.

A similar finding to the one presented here has also been reported by *Abdo et al. (2011)* based on broadband SED modelling of the source observed in 2009. Their modelling results show that the required spectral break is significantly larger than the one inferred from a simple radiative cooling scenario. As a possible explanation the authors suggest that source inhomogeneities might be responsible for the large spectral break (e.g., *Reynolds 2009*). Using a large number of *Swift*-XRT observations corresponding to different flux states, we have show here that a simple cooling break interpretation for the characteristic photon energy of Mkn 421 is inconsistent with the observations. Our statistical analysis reveals a strong anti-correlation between Γ_{low} and Γ_{high} , providing an important piece of information for identifying the physics behind the characteristic photon energy. While simple scenarios can reproduce part of the observed properties, a deeper understanding of the origin and evolution of the radiating particle

distribution is needed to satisfactorily match the observed results.

The correlation between the indices around the spectral peak might also be present for the high energy Compton spectral component if the same electron distribution is responsible for the emission at these energies and scattering occurs in the Thomson regime. However, the curvature could differ depending on the spectral shape of the target photons responsible for Compton emission. This could be further complicated if the Compton spectral peak is governed by the transition of the scattering process from the Thomson to the Klein-Nishina regime. We note that *Chen (2014)* has performed a detailed spectral study of a sample of *Fermi* bright blazars by fitting their synchrotron and Compton spectral components (one SED data set for each source) log-parabola and broken power-law functions. Comparing the sources in this sample, a significant correlation between the peak frequency and the curvature was found for the synchrotron spectral components, while the Compton spectral components did not show such a behaviour. This seems at variance with our findings based on multiple observations of a single source where no such correlation has been seen for the synchrotron spectral component. In principle, this could suggest that correlation results obtained from a single source cannot be easily generalised to the entire set of blazars. On the other hand, the results for the Compton emission are still less certain given the (then) limited observational characterisation of the Compton spectrum, and an updated analysis might be helpful to clarify the situation.

Earlier studies interpreting the blazar sequence in terms of radiative loss suggested FSRQs to undergo significant losses compared to BL Lacs (e.g., *Ghisellini et al. 2002*). This results in a rather low characteristic (peak) photon energy for FSRQs compared to BL Lacs, though the latter are more luminous. However, the present study indicates that the characteristic photon energy is not readily related to radiative losses, at least in the case of Mkn 421, and hence this inference does not apply. Therefore, a definite explanation of the characteristic photon energy along with a study based on an increase number of the sample will have the potential to decipher the mystery behind the blazar sequence.

ACKNOWLEDGEMENTS

We gratefully acknowledge the anonymous referee for very constructive comments. This research has made use of data obtained from NASA’s High Energy Astrophysics Science Archive Research Center (HEASARC), a service of the Goddard Space Flight Center and the Smithsonian Astrophysical Observatory. CB wishes to thank CSIR, New Delhi (09/043(0198)/2018-EMR-I) for financial support. CB is thankful to UGC-SAP and FIST 2 (SR/FIST/PS1-159/2010) (DST, Government of India) for the research facilities in the Department of Physics, University of Calicut.

DATA AVAILABILITY

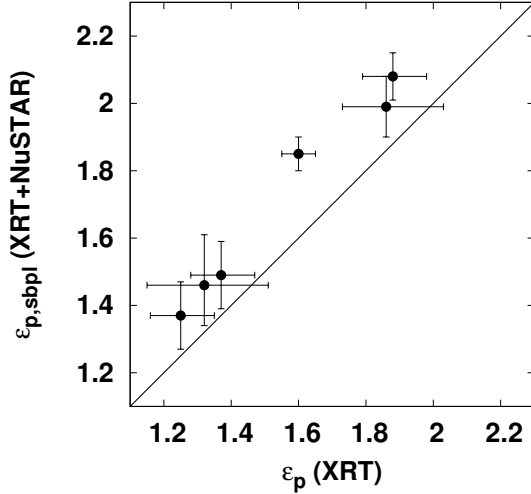
The data underlying this paper are publicly available from the HEASARC archive at <https://heasarc.gsfc.nasa.gov/>.

² <https://heasarc.gsfc.nasa.gov/>

³ <https://heasarc.gsfc.nasa.gov/docs/nustar/analysis/>

Table 2. Best fit parameters of combined (*Swift*-XRT and *NuSTAR*) spectral fitting using *sbpl* model

<i>Swift</i> -XRT ObsID	<i>NuSTAR</i> ObsID	$\epsilon_{p, sbpl}$	Γ_{low}	Γ_{high}	χ^2_{red} (dof)
80050019-Orb1	60002023027	$2.08^{+0.07}_{-0.07}$	$1.58^{+0.03}_{-0.03}$	$3.04^{+0.03}_{-0.03}$	1.06 (1303)
80050019-Orb5	60002023027	$1.85^{+0.05}_{-0.05}$	$1.68^{+0.02}_{-0.02}$	$3.08^{+0.03}_{-0.03}$	1.05 (1438)
35014065-Orb3	60002023035	$1.99^{+0.09}_{-0.09}$	$1.82^{+0.02}_{-0.02}$	$3.00^{+0.05}_{-0.05}$	1.01 (1563)
34228110-Orb3	60202048002	$1.49^{+0.1}_{-0.1}$	$1.70^{+0.04}_{-0.07}$	$2.78^{+0.05}_{-0.07}$	1.09 (1211)
34228110-Orb5	60202048002	$1.37^{+0.1}_{-0.1}$	$1.73^{+0.04}_{-0.07}$	$2.79^{+0.05}_{-0.07}$	1.04 (1201)
81926001	60202048004	$1.46^{+0.15}_{-0.12}$	$1.84^{+0.03}_{-0.04}$	$2.98^{+0.06}_{-0.08}$	1.03 (1240)


Figure 5. The scatter plot between ϵ_p and $\epsilon_{p, sbpl}$ using combined *Swift*-XRT and *NuSTAR* data, along with the identity line.

REFERENCES

- Abdo A. A., et al., 2011, *ApJ*, **736**, 131
- Acciari V. A., et al., 2009, *ApJ*, **703**, 169
- Acciari V. A., et al., 2011, *ApJ*, **738**, 25
- Aleksić J., et al., 2012, *A&A*, **542**, A100
- Arnaud K. A., 1996, in Jacoby G. H., Barnes J., eds, *Astronomical Society of the Pacific Conference Series Vol. 101, Astronomical Data Analysis Software and Systems V*. p. 17
- Baloković M., et al., 2016, *ApJ*, **819**, 156
- Bartoli B., et al., 2011, *ApJ*, **734**, 110
- Bartoli B., et al., 2016, *ApJS*, **222**, 6
- Begelman M. C., Blandford R. D., Rees M. J., 1984, *Rev. Mod. Phys.*, **56**, 255
- Błażejowski M., et al., 2005, *ApJ*, **630**, 130
- Burrows D. N., et al., 2005, *Space Sci. Rev.*, **120**, 165
- Celotti A., Ghisellini G., 2008, *Monthly Notices of the Royal Astronomical Society*, **385**, 283
- Chen L., 2014, *The Astrophysical Journal*, **788**, 179
- Dondi L., Ghisellini G., 1995, *MNRAS*, **273**, 583
- Fossati G., et al., 2008, *ApJ*, **677**, 906
- Ghisellini G., Celotti A., Costamante L., 2002, *A&A*, **386**, 833
- Giebels B., Dubus G., Khélifi B., 2007, *A&A*, **462**, 29
- Goswami P., Sahayanathan S., Sinha A., Misra R., Gogoi R., 2018, *Monthly Notices of the Royal Astronomical Society*, **480**, 2046
- Goswami P., Sahayanathan S., Sinha A., Gogoi R., 2020, *MNRAS*, **499**, 2094
- Jagan S. K., Sahayanathan S., Misra R., Ravikumar C. D., Jeena K., 2018, *MNRAS*, **478**, L105
- Kalberla P. M. W., Burton W. B., Hartmann D., Arnal E. M., Bajaja E., Morras R., Pöppel W. G. L., 2005, *A&A*, **440**, 775
- Kapanadze B., et al., 2016, *ApJ*, **831**, 102
- Kapanadze B., Dorner D., Romano P., Vercellone S., Kapanadze S., Tabagari L., 2017, *The Astrophysical Journal*, **848**, 103
- Kapanadze B., et al., 2018a, *ApJ*, **854**, 66
- Kapanadze B., Vercellone S., Romano P., Hughes P., Aller M., Aller H., Kharshiladze O., Tabagari L., 2018b, *ApJ*, **858**, 68
- Kapanadze B., et al., 2020, *The Astrophysical Journal Supplement Series*, **247**, 27
- Kardashev N. S., 1962, *Soviet Ast.*, **6**, 317
- Kataoka J., Stawarz L., 2016, *ApJ*, **827**, 55
- Katarzyński K., Walczewska K., 2010, *A&A*, **510**, A63
- Kirk J. G., Rieger F. M., Mastichiadis A., 1998, *A&A*, **333**, 452
- Krawczynski H., et al., 2004, *The Astrophysical Journal*, **601**, 151
- Mankuzhiyil N., Ansoldi S., Persic M., Rivers E., Rothschild R., Tavecchio F., 2012, *The Astrophysical Journal*, **753**, 154
- Massaro E., Perri M., Giommi P., Nesci R., 2004, *A&A*, **413**, 489
- Massaro F., Tramacere A., Cavaliere A., Perri M., Giommi P., 2008, *A&A*, **478**, 395
- Mastichiadis A., Kirk J. G., 1997, *A&A*, **320**, 19
- Press W. H., Teukolsky S. A., Vetterling W. T., Flannery B. P., 1992, *Numerical recipes in FORTRAN. The art of scientific computing*
- Reynolds S. P., 2009, *The Astrophysical Journal*, **703**, 662
- Rieger F. M., Bosch-Ramon V., Duffy P., 2007, *Ap&SS*, **309**, 119
- Rybicki G. B., Lightman A. P., 1986, *Radiative Processes in Astrophysics*
- Sahayanathan S., 2008, *MNRAS*, **388**, L49
- Sinha A., Shukla A., Misra R., Chitnis V. R., Rao A. R., Acharya B. S., 2015a, *A&A*, **580**, A100
- Sinha A., Shukla A., Misra R., Chitnis V. R., Rao A. R., Acharya B. S., 2015b, *Astronomy & Astrophysics*, **580**, A100
- Sinha A., Sahayanathan S., Acharya B. S., Anupama G. C., Chitnis V. R., Singh B. B., 2017, *ApJ*, **836**, 83
- Tramacere A., Massaro F., Cavaliere A., 2007a, *A&A*, **466**, 521
- Tramacere A., et al., 2007b, *A&A*, **467**, 501
- Tramacere A., Giommi P., Perri M., Verrecchia F., Tosti G., 2009, *A&A*, **501**, 879
- Tramacere A., Massaro E., Taylor A. M., 2011, *ApJ*, **739**, 66
- Yan D., Zhang L., Yuan Q., Fan Z., Zeng H., 2013, *The Astrophysical Journal*, **765**, 122

This paper has been typeset from a $\text{\TeX}/\text{\LaTeX}$ file prepared by the author.

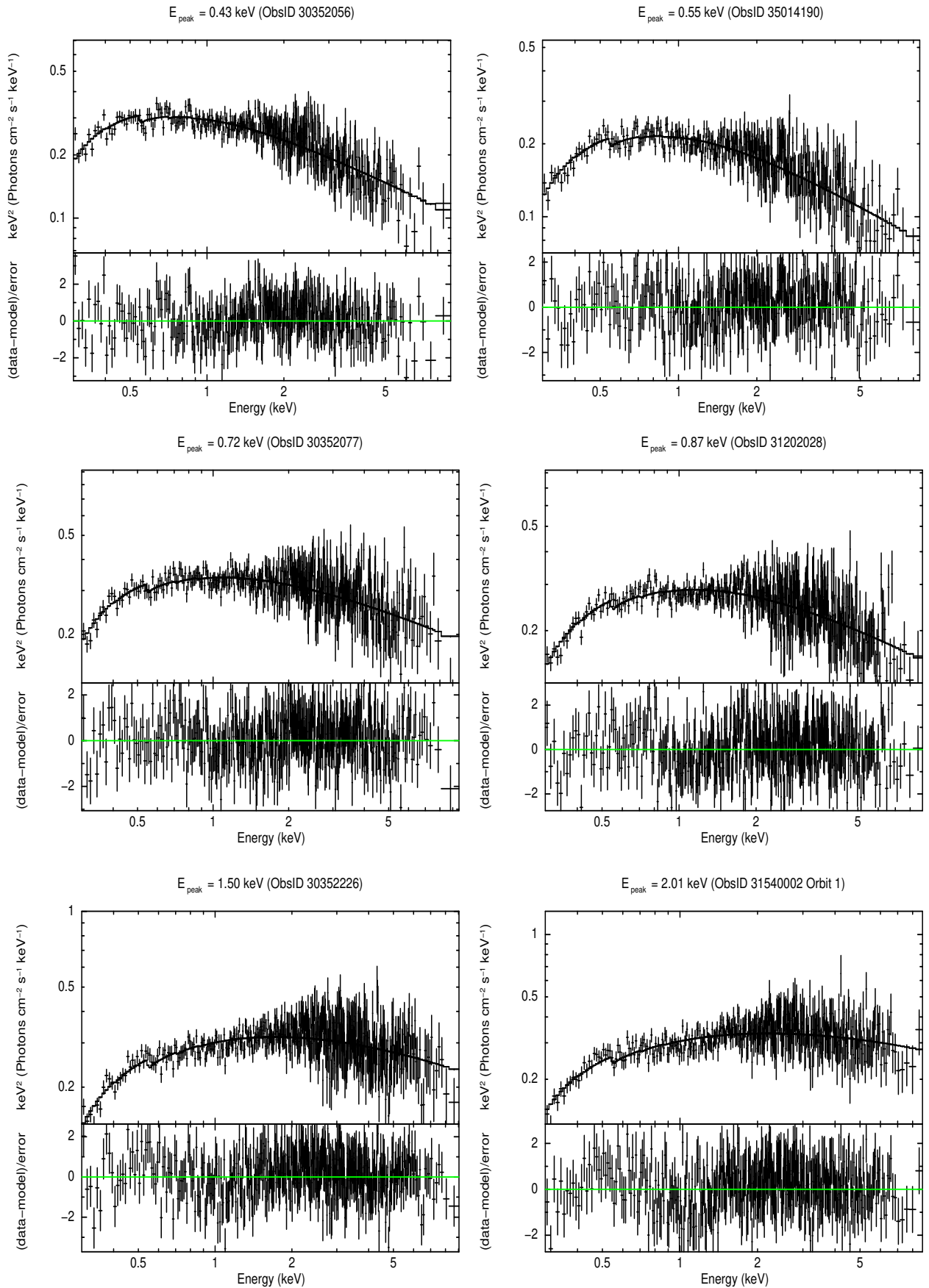


Figure 6. *sbpl* fit for observation with different ϵ_p values.